

Instrument to measure the bidirectional reflectance distribution function of surfaces

Kenneth J. Voss, Albert Chapin, Marco Monti, and Hao Zhang

A new instrument to measure the *in situ* bidirectional reflectance distribution function (BRDF) of surfaces is described. This instrument measures the BRDF for eight illumination angles from 0 to 65 deg, three colors (475, 570, and 658 nm), and at over 100 selected viewing angles. The viewing zenith angles range from 5 to 65 deg, and the azimuth angles, relative to the illumination direction, range from 0 to ± 180 deg. Many tests of the system have been run and show that for flat surfaces the BRDF of a sample surface can be measured with a precision of 1–5% and an accuracy of 10% of the measured reflectance. The BRDF for a dry and wet sand sample is presented as a demonstration of the instrument. © 2000 Optical Society of America

OCIS codes: 120.5700, 120.4640, 240.6700, 010.4450.

1. Introduction

The bidirectional reflectance distribution function (BRDF) is an important parameter to describe the interaction of light with a surface. The BRDF describes the variation of reflectance with the view and illumination direction. To define the BRDF we first need to define two other terms in radiometry. The radiance $L(\theta_v, \phi)$ is the power per unit solid angle centered in a given direction (θ_v, ϕ) passing through a unit area perpendicular to the direction (units are in $\mu\text{W cm}^{-2} \text{sr}^{-1}$). The irradiance is the power passing through a unit area, with collimated irradiance being the power in a collimated beam passing through an area perpendicular to the direction of the beam (units are in $\mu\text{W cm}^{-2}$).

The BRDF is defined as the ratio of the radiance $L(\theta_v, \phi)$ scattered by a surface into the direction (θ_v, ϕ) (see Fig. 1 for a coordinate description) to the collimated irradiance E incident on a unit area of the surface¹:

$$\text{BRDF}(\theta_i, \theta_v, \phi) = L(\theta_v, \phi) / [E \cos(\theta_i)].$$

A common simplification of the BRDF is to assume a Lambertian reflector.² With an infinite ideal Lam-

bertian reflector, illuminated uniformly, the radiance reflected from the surface is independent of the view angle and illumination direction. In this paper the data are presented as the reflectance factor $\text{REFF}(\theta_i, \theta_v, \phi)$. The $\text{REFF}(\theta_i, \theta_v, \phi)$ is defined as the ratio of the reflectance of a surface to that of a perfect Lambertian surface with the same illumination and view conditions. The $\text{REFF}(\theta_i, \theta_v, \phi)$ is related to the BRDF $(\theta_i, \theta_v, \phi)$ by a simple factor of π [i.e., $\text{REFF}(\theta_i, \theta_v, \phi) = \pi \text{BRDF}(\theta_i, \theta_v, \phi)$]. We use this factor instead of the BRDF because it is easy to quickly see the difference between the measured surface and a Lambertian reflector. Although many surfaces are assumed to be Lambertian, the reality is that few surfaces are. In general, even for surfaces that are close to Lambertian, the assumption will fail in two areas. The first obvious failure is that many flat surfaces have an enhanced specular component, i.e., an increase in the reflectance when the illumination and viewing polar angles (θ_i and θ_v , respectively) are the same, but the relative azimuth (ϕ) is 180 deg (the direction a mirror would send light). Many rough surfaces also show a reflectance enhancement in the hot-spot direction, when $\theta_i = \theta_v$ and $\phi = 0$ deg (viewing along the illumination beam). This hot spot has been seen from many natural surfaces and is a combination of many factors including a lack of shadows along this direction.³

To model the light field near a surface, the BRDF of the surface must be known. As part of the U.S. Office of Naval Research Coastal Benthic Optical Properties Program, enhanced models of the light field near benthic surfaces in the water are being devel-

The authors are with the Department of Physics, University of Miami, Coral Gables, Florida 33124. The e-mail address for K. J. Voss is voss@physics.miami.edu.

Received 27 September 1999; revised manuscript received 9 August 2000.

0003-6935/00/336197-10\$15.00/0

© 2000 Optical Society of America

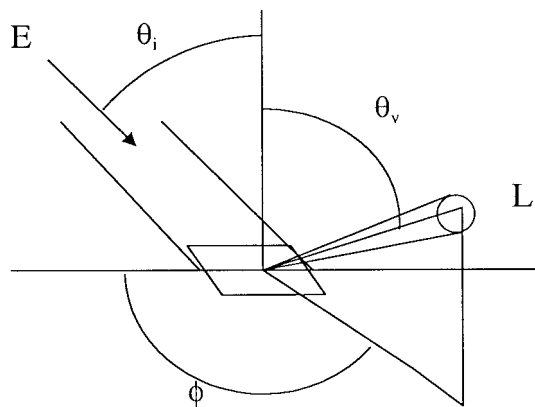


Fig. 1. Diagram of measurement geometry for BRDF. Collimated irradiance E comes in at angle θ_i . The reflected radiance is sampled at a polar angle θ_v with azimuth ϕ .

oped. Thus there was a requirement to determine accurately the BRDF for natural surfaces, such as sand.

Although the BRDF is an important factor in describing the surface reflectance, it can be difficult to measure, even for simple surfaces. Because the function varies with both illumination angle and viewing angle, many measurements are required to properly characterize a surface. Typically these measurements have been performed by an instrument with which individual measurements of viewing directions are performed for each illumination condition.^{4,5} The viewing directions and illumination conditions can be varied either manually or automatically. In either case there is a large number of individual measurements to be performed. This is time-consuming, few measurements have been performed, and these have been laboratory measurements for small surfaces. To make these measurements *in situ* for benthic surfaces requires a different design because the instrument would be operated by a scuba diver with limited air and measurement time.

We developed an instrument design that allows many viewing angles to be measured simultaneously for a specific illumination condition. With multiple illumination wavelengths and angles, the spectral BRDF can be determined in a time suitable for measurement *in situ*. This design can also be extended into the laboratory for quick, accurate characterization of both natural and man-made surfaces.

2. Instrument Description

A schematic of the instrument design is shown in Fig. 2. The two most important features of the instrument are that multiple viewing angles are measured simultaneously and there are no moving parts in the design. Illumination is provided by three colors of light-emitting diodes (LED's) which illuminate individual fibers. These fibers guide the light to a ball lens which collimates the light and directs it onto the sample surface. We select the color and illumination angle by turning on individual LED's. Re-

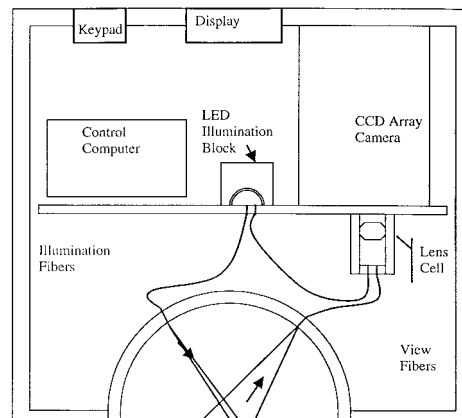


Fig. 2. Diagram of instrument design with major components listed.

flected light from the surface is collected by the view fibers, which carry this reflected light to an array. Each view fiber comes into the array at a different spot, and this array is imaged on a charge-coupled device (CCD) camera. The array is displayed in the camera image as an array of bright dots; the brightness of each dot represents the reflectance into the specific angle. The instrument housing also contains the control computer and a hard drive for data storage. The whole system can be powered by a battery, allowing remote operation. The instrument case is a 39-cm-high cylinder with a diameter of 42 cm. The specific instrument components are described below.

A. Light Source

To measure reflectance accurately one must have stable, even illumination of the surface and view this surface with a stable detector. There are two choices for the basic optical design of a reflectometer. In one of these, the surface must be illuminated over a large area, and the instrument must view a portion of the illuminated surface. This choice allows the instrument to be relatively insensitive to the distance between the receiver and the surface r_{rs} (ignoring attenuation in the path). This is because the change in the observed area of the surface that is due to a change in r_{rs} is compensated by a change in the received flux that is due to a $1/r_{rs}^2$. However, this measurement geometry requires a well-defined receiver aperture and wastes some of the illuminating beam. The second choice is to have a well-defined small illumination area and overview the surface. In this case the constraints on the receiver optics can be relaxed as it is required that only a large area, including all the illuminated area, be viewed. However, this choice is sensitive to r_{rs} because when r_{rs} is increased, the increased area viewed by the receiver is not illuminated. Even with this consideration, our design uses this geometry because we have many receivers (of the order of 100), and it is more efficient to control the illumination optics than the receiver optics.

Illumination is provided by blue, green, and red LED's [Panasonic LNG992CFBW, Lumex SSL-LX1001333XGC, and Panasonic LN261CAL(UR), respectively]. There are separate LED's for each illumination angle (θ_i) from 0° to 65° ($0^\circ, 5^\circ, 15^\circ, 25^\circ, 35^\circ, 45^\circ, 55^\circ, 65^\circ$). A 1-mm plastic fiber is used to carry the light from the illumination block to a ball lens which produces the collimated light that illuminates the sample surface. We wanted the illuminated area to be the same for each LED color, so we could not have a separate fiber for each color at a specific θ_i because multiple fibers at the focal plane of the ball lens would be directed into different directions. To get the light from three LED colors into the illumination fiber, a cavity was made in the illumination block to allow the three LED's, for a specific θ_i , to point at the tip of the fiber. The cavity was made from polished aluminum; and, although the fiber was not illuminated as efficiently as it would be for a single LED, it does allow a single fiber to be used for each illumination angle.

The light from the fiber is collimated with 10-mm BK-7 ball lenses (Edmund Scientific). The fibers are arranged so that the center of the illuminated spot on the sample surface remains constant, independent of illumination angle. There is a small change of the illuminated surface that is due to the circular spot becoming oval with increased illumination angle. The light from the ball lens exits through a hemispherical window over the sample area. We used a 20-cm-diameter compass dome (Rule Industries) as the system window. The size of this hemisphere involves several competing factors. The larger the dome, the less likely that the measurement will be affected by multiple reflections. Also, large sizes are preferred as deviations of the sample height are less critical because these affect the measurement by the inverse square of the relative change in distance. Unfortunately the ultimate instrument size is critically dependent on the size of this dome, and for diver-operated instruments, the smaller the better. Also, large dome sizes require longer path lengths through the medium, hence the opportunity for greater attenuation of the illumination and reflected light in the medium because the dome is flooded. The 20-cm compass dome was a reasonable compromise between these factors. As the illumination goes through the dome normal to the surface, and the curvature of the dome is small, there is little change in illumination spots between air and water measurements because of the refractive index of the measurement medium (dome and air or dome and water).

B. Viewing Optics

The sampling area is in the center of the hemisphere. An anodized aluminum ring is located at this position and helps maintain the sample location and height for uneven surfaces. We used 465- μm core acrylic fibers to view the sample surface. On the instrument side of the compass dome a 19-mm-thick dome of aluminum was machined to hold the illumination collimation optics and the receiver fibers. Holes

were drilled in the dome pointed at the center of the sample area. These holes were drilled at the polar angles of $5^\circ, 15^\circ, 25^\circ, 35^\circ, 45^\circ, 55^\circ, 65^\circ$. They were also dispersed azimuthally, with a concentration of measurement locations in the forward (specular) and backward (hot-spot) directions as this was anticipated to be an important feature of many surfaces. Hence azimuthal angles (ϕ) measured are $\pm 5^\circ, \pm 10^\circ, \pm 15^\circ, \pm 30^\circ, \pm 45^\circ, \pm 60^\circ, \pm 75^\circ, \pm 90^\circ, \pm 105^\circ, \pm 120^\circ, \pm 135^\circ, \pm 150^\circ, \pm 165^\circ, \pm 172^\circ, \text{ and } \pm 180^\circ$. At the smaller polar angles some of the azimuthal angles are missing because they physically interfere with the illumination optics. All the available spaces on this grid were drilled, and choices were made about which 100 viewing directions would be used. We concentrated on the forward and the backward directions and spreading the available fibers in the plus and minus azimuthal directions so that the sample symmetry could be determined. For many natural, *in situ* samples this symmetry could not be assumed.

Illumination and view fibers are limited to polar angles $< 65^\circ$ because of mechanical constraints. Because we were concerned with natural surfaces that have randomly oriented facets, if any facets at all, we expected the largest peaks to be in the hot-spot or specular direction. Thus we had view fibers at the same polar angles as the illumination fibers, and we tried to concentrate the measurements in the forward and the backward directions. Because we have discrete sampling directions we may miss sharp reflection features. But two factors make this less important. First, with the natural samples it is less likely that we will have sharp reflection features other than in the specular and hot-spot directions. Second, the data from this instrument will be used predominantly in models with less angular resolution than our measurements. Thus we do not consider that our resolution limits the applicability of our data significantly.

The fibers have a numerical aperture of 0.58. The angular collection efficiency is described in Section 5. These fibers were led from the collection dome into a fiber array block. We then imaged this block onto a Peltier-cooled CCD camera (First Magnitude Corporation) using a 16-mm lens system. Each fiber is imaged onto a 16-pixel-diameter spot on the camera. The camera cooling allowed low-noise imaging of the fiber block and also a large dynamic range (16-bit dynamic range for digitization) for the signal. A mechanical shutter, provided with the camera, was used to control acquisition time. Along with the viewing fibers, a fiber was led from each illumination cavity to the fiber array block. This could be used to verify which illumination fiber was on during the measurement and provide a convenient normalization of the data because it was proportional to the light incident on the sample. It was also used to check the stability of the camera, the LED's, and the operation of the camera shutter.

C. System Control

Control of the system is provided by an embedded 486 computer. Two two-line displays provide feedback to the diver (operator) of several instrument parameters (instrument temperature, supplied voltage levels, maximum and minimum counts in images, file names, etc). A numeric keypad is placed on the front of the case to allow the diver to control important parameters during operation of the instrument. A 2.5-in. (6.3-cm) notebook hard drive (2 Gbytes) stores the images in the instrument. A multiple channel analog-to-digital board on the computer allows instrument parameters to be measured, and a digital input-output board controls the line displays and switches the illumination LED's on and off. A custom program controls data acquisition, allowing the diver to modify exposure times and illumination sequences.

The whole system is powered from an external source. We have several choices depending on the measurement situation. The instrument is powered from a 24-V source and requires between 25 and 50 W. Thus we can use a neutrally buoyant instrument cable and a dc power supply (either a surface battery or wall power if 115 V are available). We also have battery packs that can be attached to the instrument allowing operation independent of the instrument cable. This is more convenient for in-water use; however, it increases the in-air weight of the instrument for laboratory use.

3. Data Acquisition

A full measurement sequence consists of three ambient images (measurements with no LED turned on to measure the background light leakage), 24 data images for the three colors and eight illumination angles, and three more ambient images. The total data set for one sample then consists of 30 images, 750 kbytes/image or approximately 22 Mbytes/set. After a day of measurement, we downloaded the data by transferring the data from the internal computer to a notebook computer by a twisted-pair Ethernet link. Because the important data are really an array of approximately 110 spots of illumination (rather than a 768×512 pixel image), data are subsampled prior to the transfer process, reducing the data set from 22 Mbytes to 64 kbytes. One full image is transferred along with the position file used in the subsampling to allow validation of the data reduction process before the raw data are deleted from the internal hard disk.

4. Data Reduction and Calibration

Data reduction takes place in two stages. The first stage takes place on the internal computer in the device, to reduce the size of the data set, before it is transferred to the notebook computer. The image of the fiber array block appears as an array of bright spots approximately 16 pixels in diameter. To abstract this value for a given viewing direction, the

average pixel value in this spot is used. Two unilluminated portions of the image are used to find an average dark pixel value for the image which is subtracted from the data image during the initial processing. Therefore the array transferred from the internal computer is the average pixel value for a given viewing direction with an estimate of the dark value subtracted. Because there are approximately 200 pixels averaged to obtain this spot measurement, random image noise is greatly reduced. When an unilluminated sample is reduced, the typical dark-spot average value is significantly less than one count after this process.

After the subsetted array is transferred to the other computer, the final processing is performed on the notebook computer. The first step is to subtract an average of the six ambient images collected from each data set array. This process has two effects: It accounts for any light leaks of ambient illumination into the measurement chamber and it also accounts for residual position-dependent differences in the dark values of the spots. The next step is to multiply the data arrays by an array that corrects for the relative collection efficiencies of the individual viewing channels. A description of the process to obtain these calibration arrays is given below. For a given illumination angle and color, the viewing channels are divided by the illumination intensity obtained from the fiber which samples the illumination chamber. Finally the array is multiplied by an absolute calibration number, correcting for the relative collection and collimation efficiency of the specific illumination angle and color. Thus in the end there are three arrays required for data reduction. The first is the associated ambient image, the second is an effective flat fielding of the viewing channels, and the third is a 24-element array with an absolute calibration factor for each illumination angle and color.

The later two arrays needed for data reduction are obtained during the calibration process. Calibration of the device is done through comparison with a sample of known BRDF characteristics, in our case a 99% reflectance Spectralon plaque. We measured the BRDF of this plaque for normal-incidence light in both air and water using a spectral gonio reflectometer.⁶ The results of these measurements are shown in Fig. 3. The BRDF air measurements were compared with other published measurements of Spectralon BRDF, and these measurements were found to agree well.^{7,8} The in-air and in-water measurements varied slightly, and the appropriate measurement is used during the calibration process. For $\theta_v \geq 15$ deg, the air reflectance values were fit to the polynomial

$$\text{BRDF}(\theta_i = 0, \theta_v) = 0.9686 + 0.001976\theta_v - 6.470 \times 10^{-5}\theta_v^2,$$

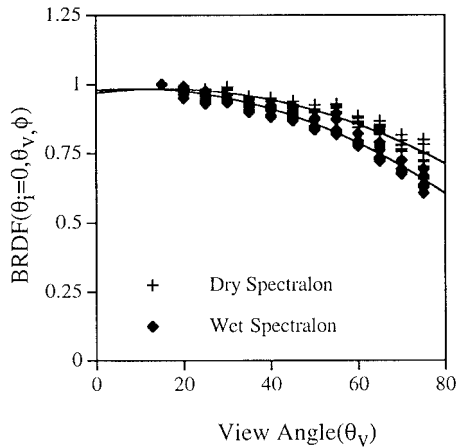


Fig. 3. Measured Spectralon BRDF values used in the calibration. Values are given for both air and water (submerged). The Spectralon plaques are the nominally 99% reflectance plaques. Curves are fits to the data described in the text.

whereas for water the reflectance was fit to the equation

$$\text{BRDF}(\theta_i = 0, \theta_v) = 0.9792 + 0.0012770\theta_v - 7.430 \times 10^{-5}\theta_v^2.$$

These equations each fit the data with a standard deviation of 0.3%. As the water quality changes, the attenuation of the viewing and illumination beams in the measurement cavity will change slightly. This is checked by our performing measurements with the calibration plaque *in situ*.

For calibration of the device, ten full measurement sets of the Spectralon plaque are made for both air and water because measurements are desired in both media. Between each measurement set the Spectralon plaque is rotated 90 deg to eliminate any orientation biases of the Spectralon surface. The ten sets of measurements are reduced through the above data reduction process but with the absolute and relative calibration arrays set to 1. Because we know the BRDF for normal illumination for this spectralon surface we can use the normal illumination measurements to derive the flat-field array. We assume (and tested) that the Spectralon surface BRDF is independent of wavelength over the wavelengths relevant to our measurement, so we use a combination of the three colors of normal illumination as the flat-field sample. Once this flat-field array is known the calibration data are rereduced with this information.

The absolute calibration array for the various θ_i and colors can be determined at this point. We use reciprocity of the reflectance from the Spectralon surface, i.e., if θ_i and θ_v are switched, the reflectance should remain the same.⁹ We know how the Spectralon surface behaves for $\theta_i = 0^\circ$; thus for $0^\circ \leq \theta_i \leq 65^\circ$ we average $\theta_v \leq 20^\circ$ to make the $\theta_v - \theta_i$ ($\theta_v = 0^\circ$) pair with which to compare with $\theta_i = 0^\circ$ and $65^\circ \geq \theta_v \geq 0^\circ$. This can then be used to derive an absolute calibration number for each color and illumination angle image.

5. System Tests and Characterizations

In this section we discuss several tests and characterization experiments that we performed with the instrument. We performed many characterization experiments, such as system linearity and spectral calibrations that help define our measurements. In addition we performed tests in which the sample location varied, which determines the final accuracy of the measurement and the limitations of the technique. These tests are described below.

A. Spectral Calibration

We measured the spectral output of the LED's using a spectroradiometer with 1-nm resolution (Optronics 740A). The red and green LED's were consistent; however, the blue LED's seemed to fall into two groups both in intensity and in spectral emission. We selected the group of blue LED's which gave the greater intensity to be used in the instrument. The central wavelength (and standard deviation) of the blue, green, and red LED's were found to be 474.8 (2.5), 569.8 (0.8), and 657.6 (1.8) nm, respectively. The FWHM (and standard deviation) of the output light was found to be 31.7 (1.3), 28.8 (0.3), and 24.1 (1.3) nm for the blue, green, and red LED's. Addition of the spectral attenuation of pure water¹⁰ significantly changes only the red LED's characteristics. For this LED the central wavelength moves to 654 nm, and the FWHM narrows to 20 nm.

B. Illumination Spot Size

The illumination spots were examined carefully. The illumination optics form circular spots on the sample surface approximately 1.3 cm in diameter for the normal-incidence spot. As θ_i increases, the spot becomes elongated, maintaining the same width but increasing in length to 3.5 cm at 65 deg. Spot size and location are independent of color because all colors use the same fiber to transfer light to the collimation ball lens. The spots from each θ_i also overlap on the sample surface and are centered within 2 mm.

C. Viewing Fibers

The acceptance efficiency of the viewing fibers was measured as a function of angle in air. These data can be fit by a Gaussian function of the form $A \exp[-(\theta/20.64)^2]$. Because of refraction at the window-water interface, the width of this curve is narrower in water. For water the corresponding fit is $A \exp[-(\theta/15.22)^2]$. The size of the dome (approximately 20 cm in diameter) and the size of the illuminated spot (1.3–3.5 cm in diameter) result in the illumination subtending a full angle of 7–20 deg for the viewing fiber for a view of 0-deg zenith. For this geometry the edge of the illuminated spot has a collection efficiency of 0.97 (0.95)–0.77 (0.64) for air (water). For $\theta_v > 0^\circ$ the viewed area gets bigger, and the illuminated spot is viewed more efficiently.

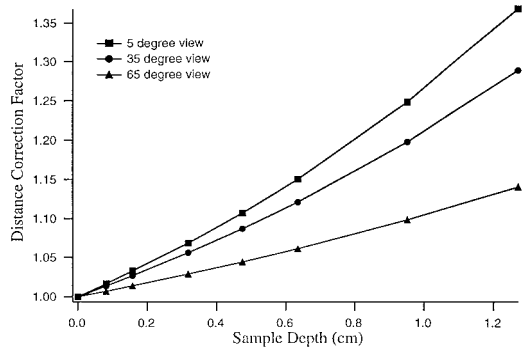


Fig. 4. Correction factor for sample depth as a function of θ_v . This factor is predicted by the given sample depth and was applied to the data in Figs. 5–7.

D. Variation with Sample Depth

Because we chose a geometry in which the illuminated area is overviewed, our measurement is dependent on sample height through a $1/r_{rs}^2$ dependence. To investigate this sensitivity to sample location we performed a test in which a Spectralon plaque was lowered away from the correct position in steps, and a measurement set was collected in each position. The data were corrected for the expected $1/r_{rs}^2$ dependence. This factor is dependent on θ_v as it has the greatest effect at $\theta_v = 0^\circ$ (relative change in r_{rs} versus sample depth is greatest here) and decreases

with increasing θ_v . For a sample depth of 1.2 cm, this factor ranges from 1.35 to 1.10 as θ_v changes from 5° to 65° , as is shown in Fig. 4. Figures 5–7 illustrate the residual dependence of the reflectance measurement on sample depth, illumination angle, and view angle. Each measurement set at a specific depth was first normalized to the measurement at 0-cm depth (the correct position). Figure 5 represents the average of all ϕ values with $\theta_v = 5^\circ$ as a function of θ_i . If this was the only factor affecting the reflectance measurements, Figs. 5–7 should be flat. The additional roll-off of the reflectance with sample depth can be accounted for by the change in the spot location and the coincidence of the viewing spot with the illumination spot. As can be seen in Fig. 5, for $\theta_i < 45^\circ$ and $\theta_v = 5^\circ$, the error is quite small regardless of sample depth. In this case the illumination spot and viewed spot retain their coincidence. As one increases θ_i to 65° , the spot effectively moves off of the center. If the sample surface is 1.2 cm deeper than the correct position, the center of the illumination spot moves over 2.6 cm. This is approximately two diameters of the spot and moves the illumination center to a view angle of 15° . This drops the collection efficiency of the viewing fiber to 60% and explains the reduction observed in this test. What this indicates is that the sample must be located correctly within 0.5 cm for a measurement error less than 10%. If the distance to the sample

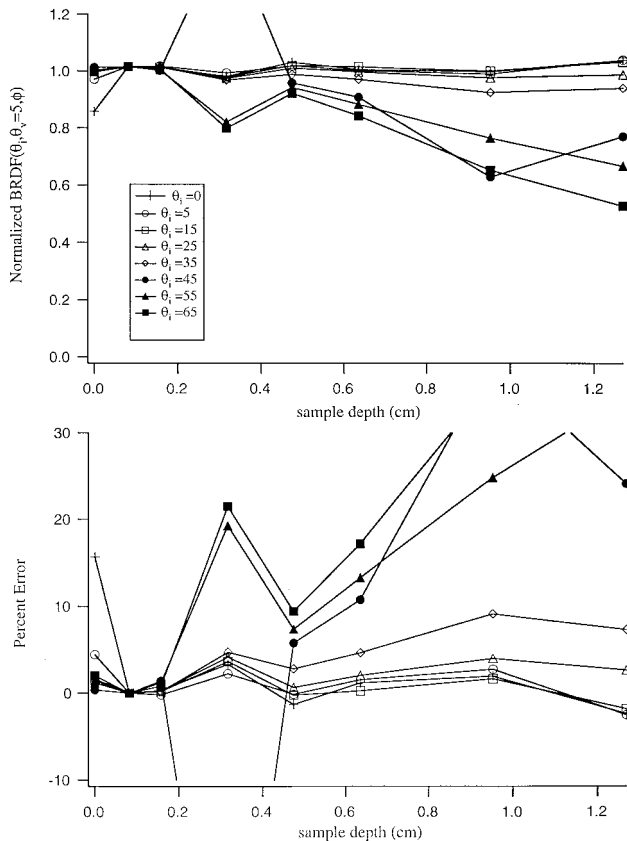


Fig. 5. Normalized BRDF and percent error in the BRDF as a function of sample depth and θ_i for $\theta_v = 5^\circ$.

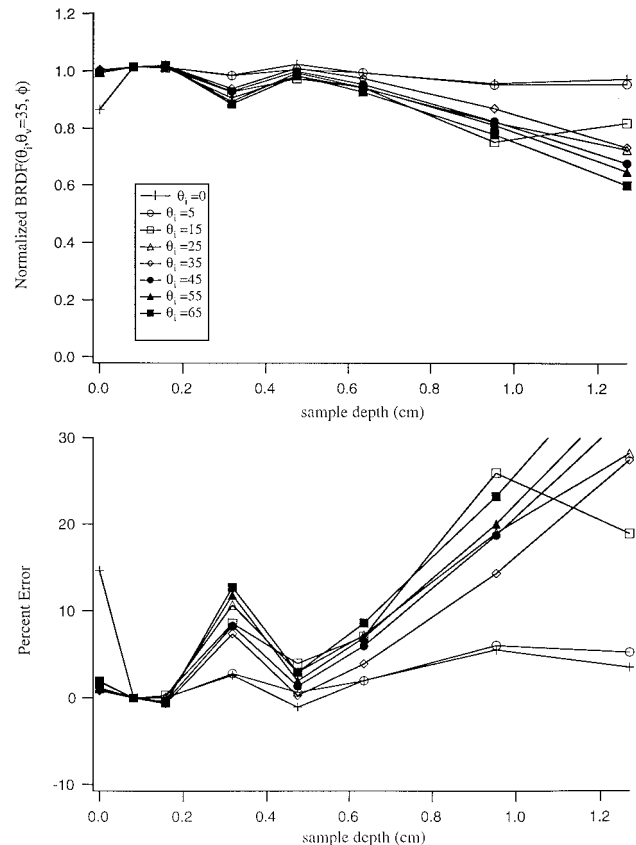


Fig. 6. Normalized BRDF and percent error in the BRDF as a function of sample depth and θ_i for $\theta_v = 35^\circ$.

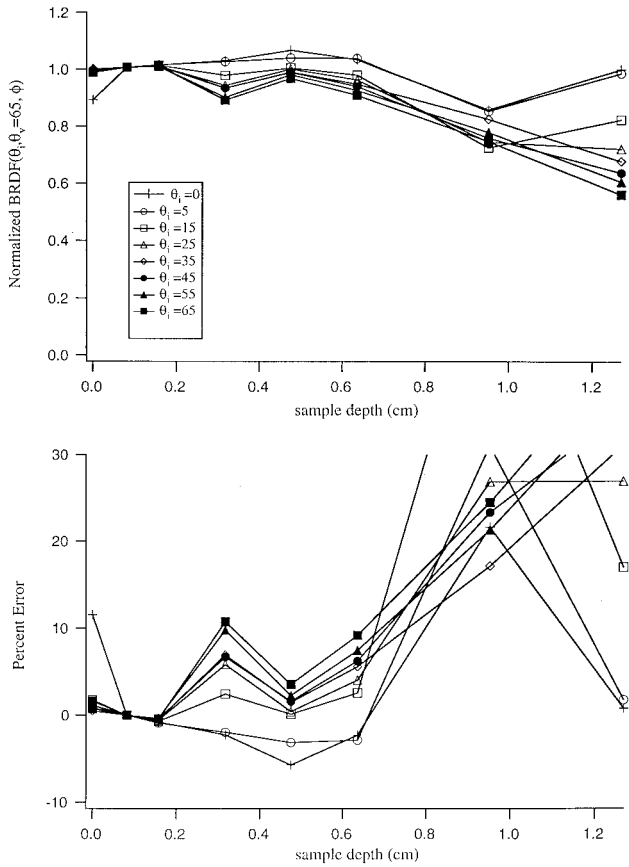


Fig. 7. Normalized BRDF and percent error in the BRDF as a function of sample depth and θ_i for $\theta_v = 65^\circ$.

cannot be estimated, the error is of the order of 20% from this effect for surface variations of 0.5 cm.

E. System Linearity

The next portion of the system response to test is the linearity of the system to flux from the sample plane. A thin sheet of diffusing material (drafting vellum, 0.6 mm thick) was placed at the location of the sample surface, and this diffuser was illuminated from the back by a stable light source. The position of the light source was varied to change the illumination on the back of the diffuser and act as a light source for the BRDF system. The data were extracted for each spot (view fiber), and these data were normalized to be able to look at the combined linearity for all the view directions. Figure 8(a) shows this combined response versus incident flux. Figure 8(b) is the percent error difference between the system response and linearity. The standard deviation of the error in the response from linearity was 5%. Some of the standard deviation is due to how the data were combined to form the total data set. As can be seen there is also greater error at the high end of the incident flux, where some pixels were starting to saturate, and at the low end, where dark-noise variations may be an appreciable portion of the signal. In general the system shows good system response for nearly 3 orders of magnitude of flux.

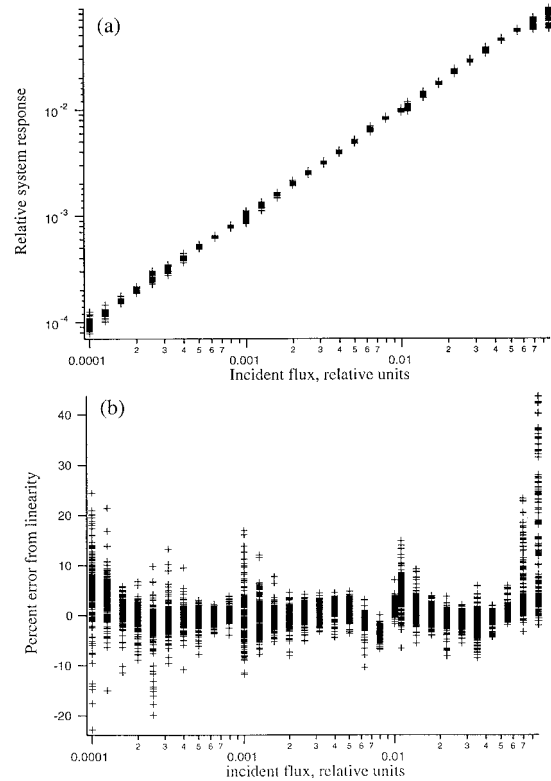


Fig. 8. (a) System linearity and (b) percent error from linearity. System is linear over 3 orders of magnitude of response. Multiple data points are the results from each of the fiber viewing spots.

F. System Stability

As a total system test, a Spectralon calibration reflectance plaque (nominally 99% reflector) was measured nine times. Between each measurement the sample was rotated to avoid orientation effects of the

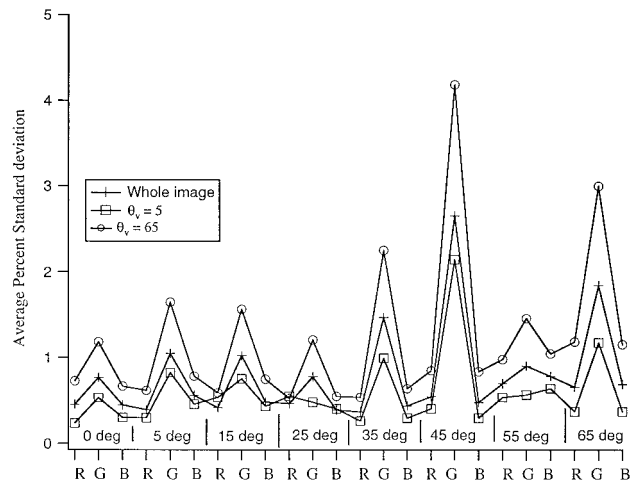


Fig. 9. Standard deviation of repetitive measurements of a Spectralon plaque. The plaque was measured nine times, with a rotation between each measurement. Data points are the average standard deviation for a whole image, $\theta_v = 5^\circ$ and $\theta_v = 65^\circ$. Each set of vertical points is for a different illumination angle and LED color. Illumination angle sets are shown on the graph; colors for each set vary from red (R) to green (G) to blue (B) from left to right.

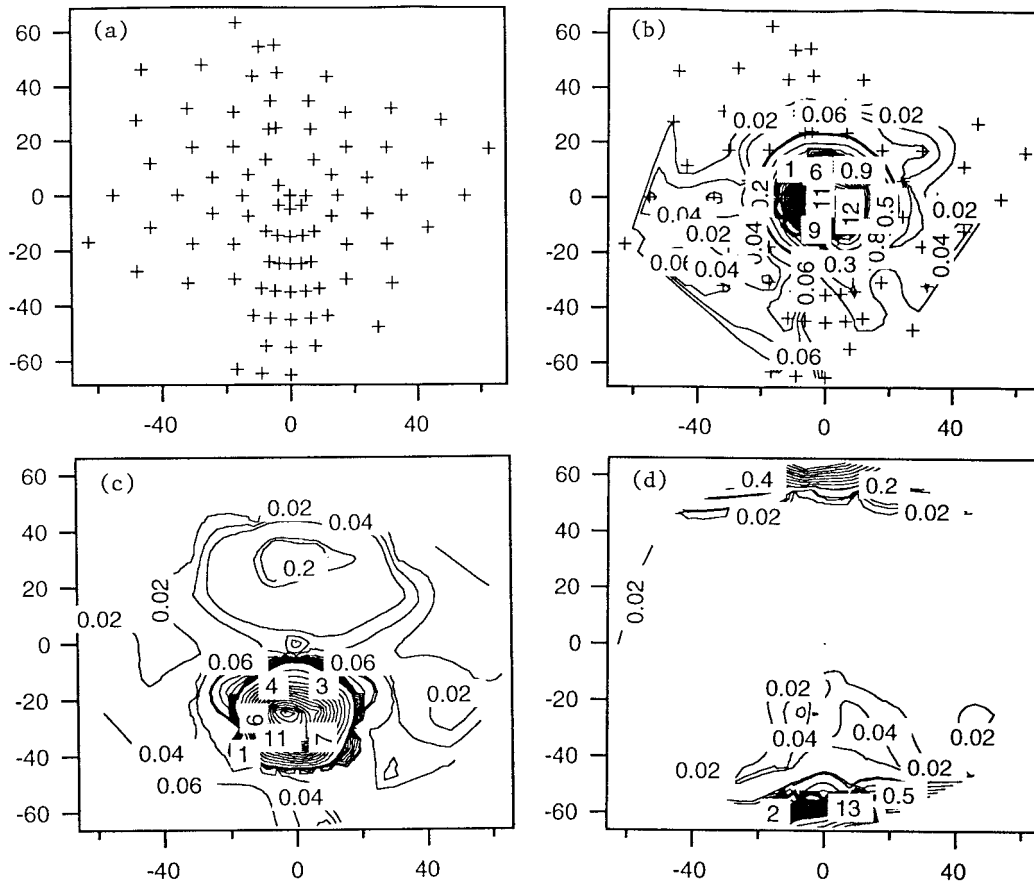


Fig. 10. REFF polar plots of a mirror surface. (a) Polar plot illustrating the location of the view fibers. Each + corresponds to a view direction. The plot is orientated such that the middle (0,0) is looking normal to the surface. Descending along the y axis corresponds to the specular direction. Ascending along the y axis corresponds to the backscattering directions (toward the illumination beam). Note the increase of samples in the specular and backward directions. (b) Normal-incidence, red LED sample shows a large increase in reflectance directly upward. Peak value was 2600%. (c) $\theta_i = 25^\circ$, red LED shows a large peak in the specular direction (1700%) and a small peak in the back direction (20%). (d) $\theta_i = 65^\circ$, red LED also shows a large peak in the specular direction (4300%) and a relatively small peak in the back direction (100%).

Spectralon. When the data were reduced, the standard deviation was found for each illumination angle and color. In Fig. 9 the average standard deviations for the total image, $\theta_v = 5^\circ$ and $\theta_v = 65^\circ$, are shown. These points are displayed as θ_i and the colors are varied. The first point on the left is the normal illumination, red LED. The points move from red to green to blue as one moves from left to right. Illumination angles are listed on the graph. Several features should be noted in this figure. First, the standard deviations are less than 5% for all cases, and the average for the whole images are less than 3%. Second, the standard deviation is largest for the green LED. This is the weakest LED, thus the signal-to-noise ratio is smallest for this wavelength, increasing the standard deviation between measurements. The standard deviation is largest for $\theta_v = 65^\circ$. This is once again because the signal tends to be less at large θ_v , causing a decrease in the signal-to-noise ratio. There is a slight increase in the standard deviation with increasing illumination angle, but this trend is not clear. Finally the standard deviations for the red and blue LED channels are sim-

ilar. If the green LED channels are excluded, the standard deviation of the measurements is less than 1%, showing that the instrument can make precise measurements of the BRDF of surfaces.

G. Sensitivity to Spurious Reflections

As a final test we show Fig. 10, which is the REFF for several illumination angles and the red LED. The sample measured is a normal front surface mirror. Figure 10(a) is a polar plot, showing the positions of the 107 viewing fibers that we have in the instrument. For orientation, the (0,0) position is looking straight down at the surface. The illumination comes in along the vertical direction above the 0° on the y axis. The polar angle moves outward from the center radially and is proportional to the radial distance from the center. We observe the increasing polar angle, in the specular direction, by moving vertically downward (negative angles along the y axis). Contours for this sample are at every 0.02 for $\text{REFF} < 0.1$, 0.1 for $0.1 < \text{REFF} < 1$, 1 for $1 < \text{REFF} < 20$, and 5 for $5 < \text{REFF}$. Figure 10(b) illustrates the $\text{REFF}(\theta_i = 0^\circ, \theta_v, \phi)$ for the red LED.

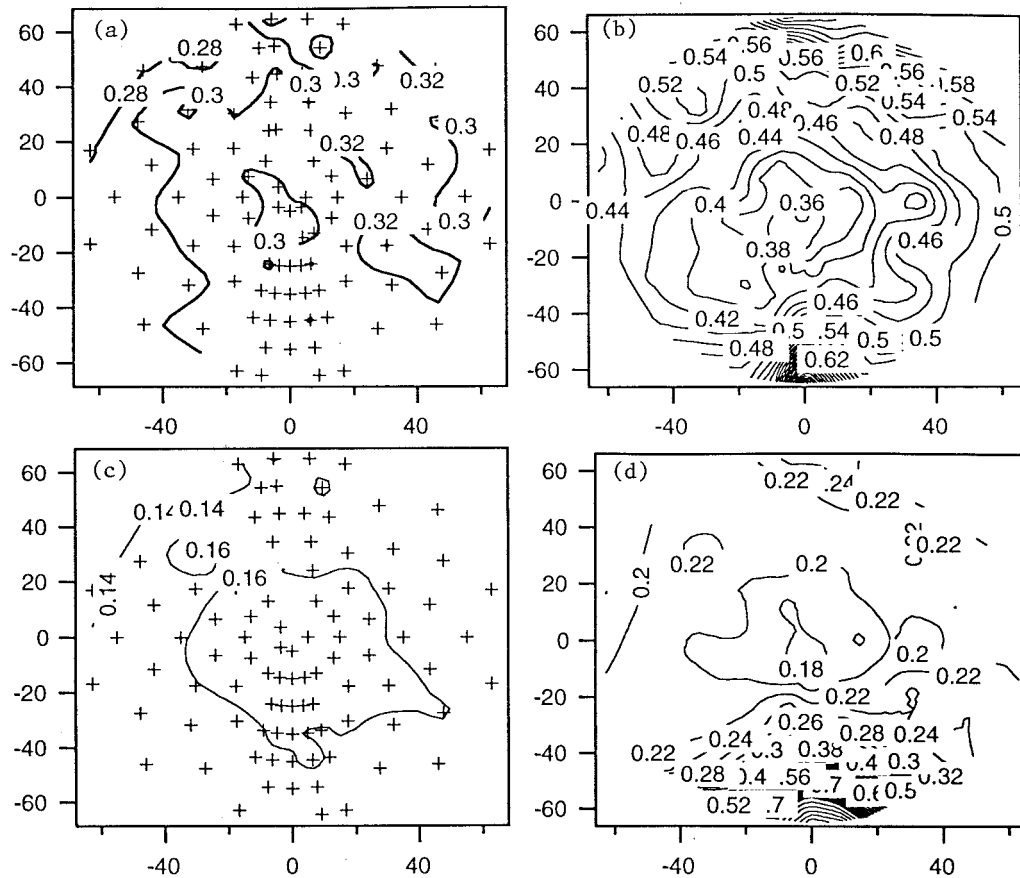


Fig. 11. REFF polar plots of dry and wet sand surfaces. (a) REFF($\theta_i = 0^\circ, \theta_v, \phi$) at 658 nm for a dry sand surface. (b) REFF($\theta_i = 65^\circ, \theta_v, \phi$) at 658 nm for a dry sand surface. (c) REFF($\theta_i = 0^\circ, \theta_v, \phi$) at 658 nm for a wet sand surface. (d) REFF($\theta_i = 65^\circ, \theta_v, \phi$) at 658 nm for a wet sand surface.

As one would expect with a mirror, there is an increase in the reflectance in the specular direction, and the reflectance is fairly symmetric around this direction. The peak value of the reflectance in this case was 26 (note that 1 is relative to a diffuse surface). Figure 10(c) is the REFF($\theta_i = 25^\circ, \theta_v, \phi$), also for the red LED. In this example the data show two peaks. The first is the specular peak (peak value observed was 17). Outside this specular peak the reflectance is low; however, there is a peak in the backward direction of 0.20. This peak is approximately 1% of the specular peak and is due to back-reflection from the window of the specular peak back down to the mirror and up to this view direction. This is the worst type of sample for this effect, and still the error that is due to this retroreflection is only of the order of 1%. Figure 10(d) is the REFF($\theta_i = 65^\circ, \theta_v, \phi$), also for the red LED. Once again the specular peak is very high (43), and the retroreflection is of the order of 2–3% of the specular peak. This data set illustrates that the instrument error that is due to internal reflection is very low, but must be considered for intensely specular surfaces. Note that in water this effect would decrease because of decreased reflectance at the water–window interface. Also a diffuse reflecting surface would spread the retroreflection down to the noise level.

6. Example Data

As an example of the measurements that we can obtain with the system, we show two examples. The first example is a sample of dry construction-grade sand. This sand appeared white when dry. Figure 11(a) shows the REFF($\theta_i = 0^\circ, \theta_v, \phi$) for 658 nm. The orientation of the graph is the same as in Fig. 10. The contours in Fig. 11(a) are at 0.02 for REFF < 1, 0.1 for $1 < \text{REFF} < 2$, and 0.2 for $2 < \text{REFF}$. As can be seen, for normal illumination, the sand sample is diffuse and Lambertian to within ± 0.02 . The lack of contours over most of the image indicates the uniformity of the sample. The nominal reflectance of the sample is 0.30 ± 0.01 . This REFF can be contrasted with Fig. 11(b), which is the REFF($\theta_i = 65^\circ, \theta_v, \phi$) for 658 nm. This sample is also dry sand, but with a large illumination angle. This sample illustrates two effects often seen in natural samples. First there is a fairly large specular peak. Although the reflectance, normal to the surface, is still approximately 0.32, the specular peak is 0.90. This sample also has an enhancement in the backscattering direction. In this direction the peak is approximately 0.70. This is the effect of the hot-spot commonly seen in BRDF's of various surfaces.³ At these larger angles of illumination the samples are clearly not Lambertian.

The next sample shown is actually the same dry sample measured above, but water was added to the sand to make the surface wet, filling the pores with water. This is not a submerged sample, but we changed the surface by adding water to the sand. Figure 11(c) is the $\text{REFF}(\theta_i = 0^\circ, \theta_v, \phi)$ for 658 nm. First it is obvious that the overall reflectance of the surface has changed significantly. In this case the nominal reflectance of the surface is 0.16 ± 0.01 . Once again the surface is Lambertian at normal incidence. This is again contrasted with Fig. 11(d) that is the $\text{REFF}(\theta_i = 65^\circ, \theta_v, \phi)$ for 658 nm for the same sample. Once again, when the surface is wet the normal reflectance is lower than in Fig. 11(b). As in Fig. 11(b), there is a large specular peak. In fact, in this case the reflectance of the specular peak has increased to 1.60, which is much larger than in the dry sand. This is probably caused by having some of the surface covered with water and is a reflection from the air–water interface. Measurement of submerged sand samples have not shown this large specular peak. The backward-scattering peak has diminished significantly from that seen in Fig. 11(b). Here the peak is only 0.24. Although this is greater than the reflectance at $\theta_v = 0$, it is still not as large an increase as seen in the dry sand.

7. Conclusion

We have described a new instrument to make relatively rapid *in situ* measurements of the BRDF of surfaces. This instrument will allow the BRDF for many surfaces to be measured and characterized for use in optical modeling of the light field and remote sensing. Our major concern when using the instrument is to make sure that the sample height is correct because the accuracy is dependent on this factor. The precision of the measurement has been shown to be 1–5%. The accuracy of the measurement is dependent on how well the surface height has been determined. If the surface is correctly placed within 0.5 cm, the accuracy is approximately 10%, depending on θ_v and θ_i (note that this is 10% of the measured reflectance value, not 10% in reflectance units).

This instrument will be used to make field measurements of the BRDF in various environments to help characterize benthic surfaces and to improve modeling and remote sensing algorithms.

The research presented in this paper has been supported by the Ocean Optics Program of the U.S. Office of Naval Research (N001499-10008). We thank Karl Moore who helped in the early development of the instrument.

References

1. B. Hapke, *Theory of Reflectance and Emittance Spectroscopy*, Vol. 3 of Topics in Remote Sensing (Cambridge U. Press, New York, 1993).
2. R. A. Leathers and N. J. McCormick, "Algorithms for ocean-bottom albedo determination from in-water natural-light measurements," *Appl. Opt.* **38**, 3199–3205 (1999).
3. J. M. Chen and J. Cihlar, "A hotspot function in a simple bidirectional reflectance model for satellite applications," *J. Geophys. Res.* **102**, 25907–25913 (1997).
4. D. R. White, P. Saunders, S. J. Bonsey, J. van de Ven, and H. Edgar, "Reflectometer for measuring the bidirectional reflectance of rough surfaces," *Appl. Opt.* **37**, 3450–3454 (1998).
5. J. R. Zaworski, J. R. Welty, and M. K. Drost, "Measurement and use of bi-directional reflectance," *Int. J. Heat Mass Transfer* **39**, 1149–1156 (1996).
6. J. W. Giles and K. J. Voss, "Submerged reflectance measurements as a function of visible wavelength," in *Underwater Imaging, Photography, and Visibility*, R. W. Spinrad, ed., Proc. SPIE **1537**, 140–146 (1991).
7. B. T. McGuckin, D. A. Haner, and R. T. Menzies, "Multiangle imaging spectroradiometer: optical characterization of the calibration panels," *Appl. Opt.* **36**, 7016–7022 (1997).
8. K. D. Moore, K. J. Voss, and H. R. Gordon, "Spectral reflectance of whitecaps: instrumentation, calibration, and performance in coastal waters," *J. Atmos. Oceanic Technol.* **15**, 496–509 (1998).
9. W. C. Snyder, "Reciprocity of the bidirectional reflectance distribution function (BRDF) in measurements and models of structured surfaces," *IEEE Trans. Geosci. Remote Sens.* **36**, 685–691 (1998).
10. R. M. Pope and E. S. Fry, "Absorption spectrum (380–700 nm) of pure water. II. Integrating cavity measurements," *Appl. Opt.* **36**, 8710–8723 (1997).